T and F asymmetries in π^0 photoproduction on the proton

J. R. M. Annand,[1] H. J. Arends,[2] R. Beck,[3] N. Borisov,[4] A. Braghieri,[5] W. J. Briscoe,[6] S. Cherepnya,[7] C. Collicott,[8] S. Costanza,[5] E. J. Downie,[2,6] M. Dieterle,[9] A. Fix,[10] L. V. Fil'kov,[7] S. Garni,[9] D. I. Glazier,[1,11] W. Gradl,[2] G. Gurevich,[12] P. Hall Barrientos,[11] D. Hamilton,[1] D. Hornidge,[13] D. Howdle,[1] G. M. Huber,[14] V. L. Kashevarov,[2,7] I. Keshelashvili,[9] R. Kondratiev,[12] M. Korolija,[15] B. Krusche,[9] A. Lazarev,[4] V. Lisin,[7] K. Livingston,[1] I. J. D. MacGregor,[1] J. Mancel,[1] D. M. Manley,[16] P. P. Martel,[2,17] E. F. McNicoll,[1] W. Meyer,[18] D. G. Middleton,[2,13] R. Miskimen,[17] A. Mushkarenkov,[5,17] A. Neganov,[4] A. Nikolaev,[3] M. Oberle,[9] H. Ortega,[2] M. Ostrick,[2] P. Ott,[2] P. B. Otte,[2] B. Oussena,[2,6] P. Pedroni,[5] A. Polonski,[12] V. V. Polyanski,[7] S. Prakhov,[19] G. Reicherz,[18] T. Rostomyan,[9] A. Sarty,[8] S. Schumann,[2] O. Steffen,[2] I. I. Strakovsky,[6] Th. Strub,[9] I. Supek,[15] L. Tiator,[2] A. Thomas,[2] M. Unverzagt,[2] Yu. A. Usov,[4] D. P. Watts,[11] D. Werthmüller,[1,9] L. Witthauer,[9] and M. Wolfes[2]

(A2 Collaboration at MAMI)

[1]*SUPA School of Physics and Astronomy, University of Glasgow, Glasgow G12 8QQ, United Kingdom*

[2]*Institut für Kernphysik, Johannes Gutenberg-Universität Mainz, D-55099 Mainz, Germany*

[3]*Helmholtz-Institut für Strahlen- und Kernphysik, Universität Bonn, D-53115 Bonn, Germany*

[4]*Joint Institute for Nuclear Research, 141980 Dubna, Russia*

[5]*INFN Sezione di Pavia, I-27100 Pavia, Italy*

[6]*The George Washington University, Washington, DC 20052-0001, USA*

[7]*Lebedev Physical Institute, 119991 Moscow, Russia*

[8]*Department of Astronomy and Physics, Saint Mary's University, Halifax, Nova Scotia B3H 3C3, Canada*

[9]*Departement für Physik, Universität Basel, CH-4056 Basel, Switzerland*

[10]*Laboratory of Mathematical Physics, Tomsk Polytechnic University, 634034 Tomsk, Russia*

[11]*SUPA School of Physics, University of Edinburgh, Edinburgh EH9 3JZ, United Kingdom*

[12]*Institute for Nuclear Research, 125047 Moscow, Russia*

[13]*Mount Allison University, Sackville, New Brunswick E4L 1E6, Canada*

[14]*University of Regina, Regina, Saskatchewan S4S 0A2, Canada*

[15]*Rudjer Boskovic Institute, HR-10000 Zagreb, Croatia*

[16]*Kent State University, Kent, Ohio 44242-0001, USA*

[17]*University of Massachusetts, Amherst, Massachusetts 01003, USA*

[18]*Institut für Experimentalphysik, Ruhr-Universität, D-44780 Bochum, Germany*

[19]*University of California Los Angeles, Los Angeles, California 90095-1547, USA*

(Received 20 March 2016; published 31 May 2016)

The $\gamma p \to \pi^0 p$ reaction was studied at laboratory photon energies from 425 to 1445 MeV with a transversely polarized target and a longitudinally polarized beam. The beam-target asymmetry F was measured for the first time and new high precision data for the target asymmetry T were obtained. The experiment was performed at the photon tagging facility of the Mainz Microtron (MAMI) using the Crystal Ball and TAPS photon spectrometers. The polarized cross sections were expanded in terms of associated Legendre functions and compared to recent predictions from several partial-wave analyses. The impact of the new data on our understanding of the underlying partial-wave amplitudes and baryon resonance contributions is discussed.

DOI: 10.1103/PhysRevC.93.055209

I. INTRODUCTION

Photoinduced meson production off nuclear targets is a powerful tool for investigating the spectrum of light baryons [1]. In $\gamma N \to \pi N$ reactions excited nucleons (N^*) and Δ^* states manifest themselves as resonances in partial-wave amplitudes. Above the $\Delta(1232)3/2^+$ ground state, resonances strongly overlap in energy, and the isolation of contributions from individual partial-wave amplitudes with fixed spin, parity, and isospin is a vital issue in baryon spectroscopy. Such a separation requires measurements of polarized cross sections with different orientations of target and beam polarization or with detection of the polarization of the outgoing nucleon.

Currently, major progress is observed due to high precision data from modern photoproduction experiments. The differential cross sections for the $\gamma p \to \pi^0 p$ reaction were obtained with unprecedented accuracy and full angular coverage at the Mainz Microtron (MAMI) [2]. New measurements of beam and beam-target asymmetries were performed by the CBELSA/TAPS experiment at the Electron Stretcher and Accelerator (ELSA) [3–6], the GRAAL experiment at the European Synchrotron Radiation Facility (ESRF) [7], and the CLAS experiment at the Jefferson Lab (JLab) [8,9]. Measurements of the polarization of the recoiling proton were performed at JLab and MAMI [10,11].

In this paper we present new results on the $\gamma p \to \pi^0 p$ reaction measured with a transversely polarized target and a longitudinally polarized beam in the photon energy region from 425 to 1445 MeV. In this case, the polarized differential

cross section can be written as

$$\frac{d\sigma}{d\Omega} = \frac{d\sigma_0}{d\Omega}(1 + P_T \sin\phi\ T + hP_\odot P_T \cos\phi\ F). \quad (1)$$

Here $d\sigma_0/d\Omega$ is the unpolarized cross section, $P_\odot$ and P_T denote the degree of beam and target polarization, $h = \pm 1$ is the beam helicity, and ϕ is the azimuthal angle of the target polarization vector in a coordinate frame fixed to the reaction plane defined by the incoming photon and final-state meson momenta, such that $\hat{z} = \vec{p}_\gamma/|\vec{p}_\gamma|$, $\hat{y} = \vec{p}_\gamma \times \vec{p}_\pi/|\vec{p}_\gamma \times \vec{p}_\pi|$, and $\hat{x} = \hat{y} \times \hat{z}$.

Sections II and III describe the experimental apparatus and the analysis methods, respectively. In Sec. IV the results for the asymmetries T and F defined in Eq. (1) are presented and discussed.

II. EXPERIMENTAL SETUP

The experiment was performed at the Mainz Microtron (MAMI) electron accelerator facility [12] using the Glasgow-Mainz tagging spectrometer [13] and the Crystal Ball/TAPS detector setup. Bremsstrahlung photons were produced by scattering a 1557 MeV electron beam with a longitudinal polarization of about 80% on a 10 μm thick copper radiator, while scattered electrons were separated from the main beam and momentum-analyzed by a magnetic dipole spectrometer (see Fig. 1). With the known beam energy E_0 and the energy E_e of scattered electrons, the emitted photon energy E_γ is given by

$$E_\gamma = E_0 - E_e. \quad (2)$$

This photon beam covered an energy range from 425 to 1450 MeV with an average energy resolution of 4 MeV.

The longitudinal polarization of the electron beam is transferred to circular polarization of the photons during the bremsstrahlung process. The photon polarization depends on the energy and varied from 35% at 425 MeV to 78% at 1450 MeV (see Fig. 2).

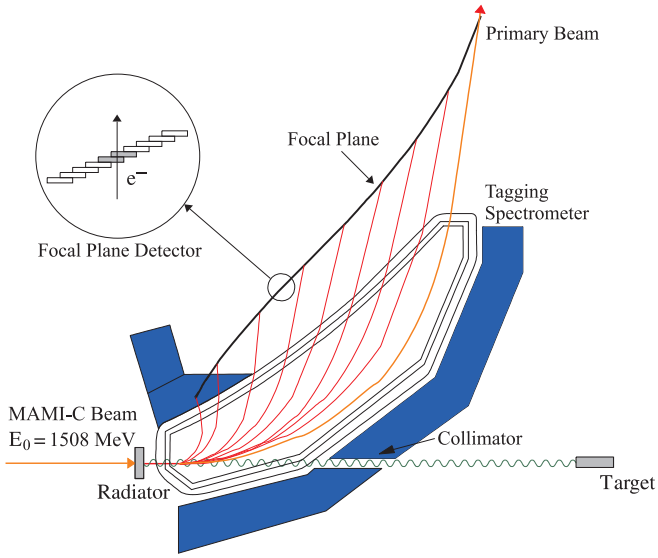

FIG. 1. The Glasgow-Mainz photon tagging spectrometer.

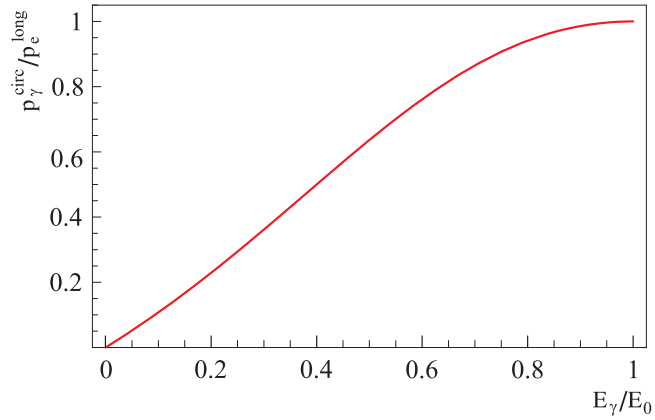

FIG. 2. Helicity transfer from the electron to the photon beam as a function of the energy transfer [14].

The detector setup is shown schematically in Fig. 3. The bremsstrahlung photons, collimated by a lead collimator, impinged on a target located in the center of the Crystal Ball detector [15]. This detector consists of 672 optically isolated NaI(Tl) crystals with a thickness of 15.7 radiation lengths covering 93% of the full solid angle with an energy resolution for electromagnetic showers described by $\Delta E/E = 0.02/(E/\text{GeV})^{0.36}$. Shower directions were measured with a resolution of $\sigma_\Theta \approx 2$–3° in the polar and $\sigma_\phi \approx 2^\circ/\sin\Theta$ in the azimuthal angle.

A barrel of 24 scintillation counters surrounding the target measures the differential energy loss of charged particles, which, together with the total energy deposited in the Crystal Ball, can be used in a $\Delta E/E$ analysis for separation of protons and charged pions [16]. In this analysis it was only used to separate charged from neutral particles.

The forward angular range $\Theta = 1$–20° is covered by the TAPS calorimeter [17], which consists of 384 hexagonally shaped BaF_2 detectors and was installed 1.5 m downstream

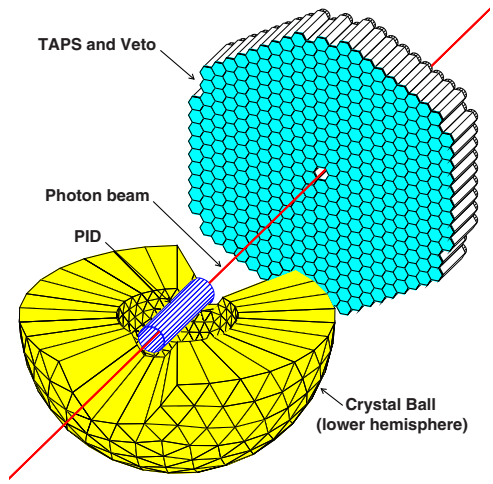

FIG. 3. Detector setup consisting of the Crystal Ball and TAPS calorimeters. The upper hemisphere of the Crystal Ball is omitted to show the barrel of plastic scintillators surrounding the target (PID).

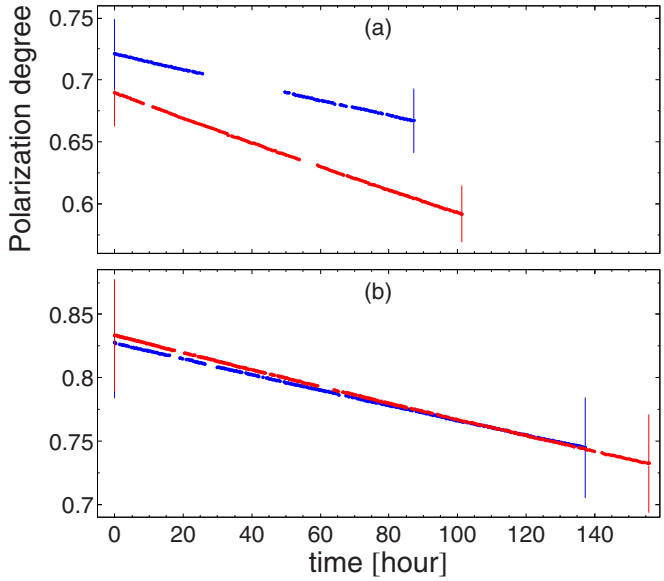

FIG. 4. Time dependence of the target polarization for the running periods in 2010 (a) and 2011 (b). The red (blue) points correspond to a polarization vector oriented upward (downward) in the laboratory system. The error bars at the beginning and end of each period indicate direct NMR measurements. The polarization degree for each run was obtained from the exponential relaxation.

of the Crystal Ball center. Each hexagonally shaped BaF_2 crystal has an inner diameter of 5.9 cm and a length of 25 cm, corresponding to 12 radiation lengths. Electromagnetic showers are determined with an energy resolution of $\sigma_E/E = 0.008/(E/\mathrm{GeV})^{1/2} + 0.018$ and angular resolutions of less than 1° FWHM [17]. A 5 mm thick plastic scintillator in front of each module allows the separation of neutral and charged particles. The solid angle coverage of the combined Crystal Ball/TAPS detector setup was approximately 97% of 4π. Further details about the experimental set up are given in Ref. [18].

Transversely polarized target protons were provided by a frozen-spin target system [19] using butanol (C_4H_9OH) as target material. The target container with a length of 2 cm and a diameter of 2 cm was filled with 2 mm diameter TEMPO-doped butanol spheres with a packing fraction ("filling factor") of 61%, resulting in a density of free, polarizable protons in the butanol target of 9.27×10^{22} cm^{-2}. A specially designed ^{3}He /^{4}He dilution refrigerator kept the target material at temperatures around 25 mK, which provided relaxation times of about 1500 h. The orientation of the proton polarization vector during the measurements was maintained by a four-layer saddle coil that provided a magnetic holding field of 0.45 T.

The target polarization was measured at the beginning and the end of each data taking period using NMR techniques. The average proton polarization during the beam time periods May-June 2010 and April 2011 was 70%. In order to reduce systematic uncertainties, the direction of the target polarization vector was reversed during the experiment, as indicated in Fig. 4. More details about the construction and operation of the target are given in Ref. [19].

III. DATA ANALYSIS

The observables T and F in Eq. (1) are defined as asymmetries between differential cross sections with different orientations of target spin and beam helicity.

In principle, they can be determined in each energy and angular bin as count-rate asymmetries from the number $N^{\pm}$ of reconstructed $\vec{\gamma}\,\vec{p} \to \pi^0 p$ events:

$$T = \frac{1}{P_T |\sin\phi|} \frac{N^{\pi=+1} - N^{\pi=-1}}{N^{\pi=+1} + N^{\pi=-1}}, \tag{3}$$

$$F = \frac{1}{P_T |\cos\phi|} \frac{1}{P_\odot} \frac{N^{\omega=+1} - N^{\omega=-1}}{N^{\omega=+1} + N^{\omega=-1}}. \tag{4}$$

Here $\pi = \vec{p}_T \cdot \hat{y}/|\vec{p}_T \cdot \hat{y}| = \pm 1$ denotes the orientation of the target polarization vector $\vec{p}_T$ relative to the normal of the production plane and, in the case of the F asymmetry, $\omega = h\ \vec{p}_T \cdot \hat{x}/|\vec{p}_T \cdot \hat{x}| = \pm 1$ is given by the product of the beam helicity h and the orientation of $\vec{p}_T$ relative to the $\hat{x}$ axis. The degree of target polarization is taken into account event by event in each of the 18°-wide azimuthal angular bins. In these asymmetries, common systematic uncertainties related to the reconstruction efficiency, the photon flux, and the target filling factor cancel. However, using butanol as target material has an essential consequence because of the background coming from quasifree reactions on ^{12}C and ^{16}O nuclei. In the numerator of Eqs. (3) and (4), this background cancels because the nucleons bound in ^{12}C or ^{16}O are unpolarized. However, in order to determine the denominator, this contribution has to be taken into account.

As the first step in the analysis, the π^0 meson was identified and reconstructed from the $\pi^0 \to \gamma\gamma$ decay. The detection of recoil protons and the requirement of coplanarity of the incoming photon and the outgoing hadrons already suppresses background from ^{12}C or ^{16}O significantly.

The residual background was subtracted using the missing mass MM(γp,π^0) calculated from the reconstructed π^0 momentum with the assumption of a free proton in the initial state. In addition to butanol, the shape of this missing-mass distribution was determined for π^0 photoproduction on a pure carbon and a liquid hydrogen target. The shapes of these distributions were then used as templates to fit the butanol data and to separate free and quasifree reactions. Since the magnitude and the shape of the background depend on the initial beam energy and momenta of the final particles, the background subtraction procedure was performed for each energy and angular bin. This procedure is illustrated in Fig. 5 for three different bins, which are typical for the presented data analysis. Missing-mass spectra obtained with the carbon target are shown in Figs. 5(a), 5(b), and 5(c) by the black histograms. The green lines represent our best fits, which are then used to describe the butanol data. The distributions measured with the butanol target are presented by the black histograms in Figs. 5(d), 5(e), and 5(f). The red line is the fit result obtained with the templates from carbon (green lines) and hydrogen (blue lines) targets. The data analysis with hydrogen target is described in detail in [2].

Only events inside missing-mass intervals indicated by the vertical solid lines were selected for further analysis. This

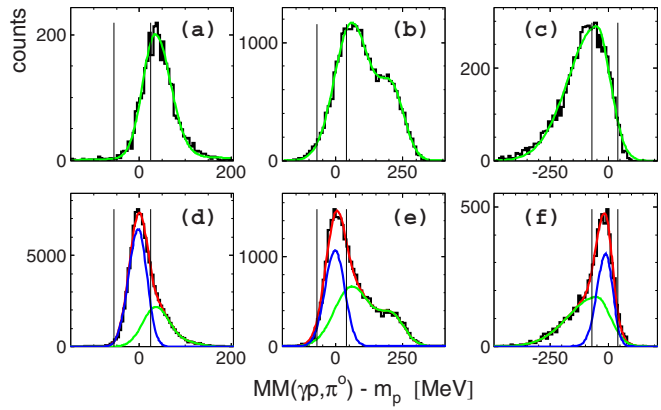

FIG. 5. Distributions of the missing mass, $\mathrm{MM}(\gamma p,\pi^0) - m_p$, obtained with carbon [(a)–(c)] and butanol [(d)–(f)] targets at $E_\gamma =$ 440 MeV, $\Theta = 65^\circ$ [(a),(d)] and $E_\gamma = 680$ MeV, $\Theta = 65^\circ$ [(b),(e)], $\Theta = 160^\circ$ [(c),(f)]. The butanol distributions can be fitted by a normalized sum of carbon (green line) and pure hydrogen (blue line). The vertical solid lines indicate the selection of $\gamma p \to \pi^0 p$ reactions used in the analysis.

range was varied and optimized to minimize the uncertainties related to the background subtraction to 3–4%. The other dominant systematic uncertainties arose from the determination of the degree of target (4%) and beam polarization (2%). By adding all contributions in quadrature, a total systematic uncertainty of less than 6% is obtained.

IV. RESULTS AND DISCUSSION

Figures 6 and 7 show the measured dependence of the asymmetries T and F on the center-of-momentum angle Θ^*_π for each of the 34 photon energy bins. The target asymmetry T agrees well with existing data [20], in particular with measurements of CBELSA/TAPS [4]. The F asymmetry was measured for the first time. The data are compared to predictions of the single-channel isobar model MAID2007 [21], the SAID PR15 [2,22] solution, the multichannel fits BG2014-2 [23] and BG2011-2 [24], and the Juelich-Bonn dynamical coupled-channel approach JuBo2015-B [25]. The oldest approach is from MAID2007, which was fitted to the limited amount of data available in 2007. Therefore, larger discrepancies are not surprising. The other models used recent polarization data from CBELSA/TAPS [3–6] as well as our precise cross-section data [2] in their fits.

Figure 8 shows the dependence on the center-of-momentum energy W for selected angular bins and the comparison to the model calculations. Here we note the difference between the BG2014-2 (black solid) and BG2011-2 (black dashed) solutions. In the BG2014-2 fit, data for T, P, and H were included that were not available when the previous BG2011-2 solution was published. This led to changes of some of the extracted multipole amplitudes, like E_{0+} and E_{1+}. An essential conclusion of [5], however, was that inclusion of the new data leads to a significantly better convergence of different fits and therefore to a less model-dependent extraction of partial-wave amplitudes. This is important because the unambiguous determination of multipoles like M_{1-}, M_{2+}, or E_{2+} is a prerequisite for the unique determination of baryon resonance parameters. It is instructive to see if the new BG2014-2 parameters also lead to a better description of other observables that were not included in the fit. Figure 8 shows that BG2014-2 indeed provides a better description than BG2011-2 of the beam-target asymmetry F in the whole energy range even though this observable was not used to constrain the model. This observation may be viewed as an indication that different phenomenological models indeed converge when the number of the observables used in the fit and the quality of their measurements increases.

In order to analyze our new data more deeply, we expanded the polarized cross sections $T\, d\sigma/d\Omega$ and $F\, d\sigma/d\Omega$ in terms of associated Legendre functions of the first order,

$$\mathcal{O}\,\frac{d\sigma}{d\Omega} = \sum_{n=1}^{N} A_n^{\mathcal{O}} P_n^1(\cos\Theta^*_\pi), \quad \mathcal{O} = T, F. \tag{5}$$

The coefficients $A_n^{\mathcal{O}}$ can be determined from a least-squares fit to the data. The maximum order N, to which the expansion has to be truncated, depends on the underlying dynamics as well as on the quality of the data.

In order to perform this analysis the polarized cross sections $T\, d\sigma/d\Omega$ and $F\, d\sigma/d\Omega$ were obtained by interpolating and averaging our cross-section data [2] to the energy and angular bins used for the asymmetries T and F. The resulting unpolarized and polarized differential cross sections are shown in Fig. 9 for selected energy bins together with Legendre-expansions truncated to different values of N. Only the statistical uncertainties were used for the fits. It was observed that including Legendre functions beyond $N = 6$ in the fits could not significantly improve the reduced χ^2. The comparison of the reduced χ^2 for the fits of the data with $N = 4$, 6, and 8 is shown in Fig. 10. In the energy range below $E_\gamma = 0.8$ GeV, fitting with $N = 4$ can be expected to be sufficient for a good description of the polarized differential cross sections. In the high energy region $E_\gamma > 1.1$ GeV, a significant difference between the fit results with $N = 6$ and 8 at forward angles is observed (see blue and black lines in Fig. 9). Additional measurements at the forward angles are needed to clarify these contributions from high angular momenta. It should be stressed that a truncated expansion in terms of a finite number of terms [Eq. (5)] leads to a satisfactory description of the data. This observation is related to the fact that background terms, which produce a large number of high partial waves in, for example, the $\gamma p \to \pi^+ n$ reaction, are small in π^0 production. Therefore, baryon resonance contributions can be qualitatively discussed at this level. In the expansion of Eq. (5), an isolated resonance with spin J will only contribute to even coefficients with $n < 2J$. The interference of two resonances with equal parities appears only in coefficients with even values of n; those with different parities only in the terms with odd values of n.

Our results for the energy dependence of the coefficients $A_n^{T/F}$ are plotted in Figs. 11 and 12. In general, this analysis confirms the observation that BG2014-2 provides a better description of the beam-target observable F that the previous BG2011-2 fit. Nevertheless, there are still some discrepancies in A_4^T and A_5^T.

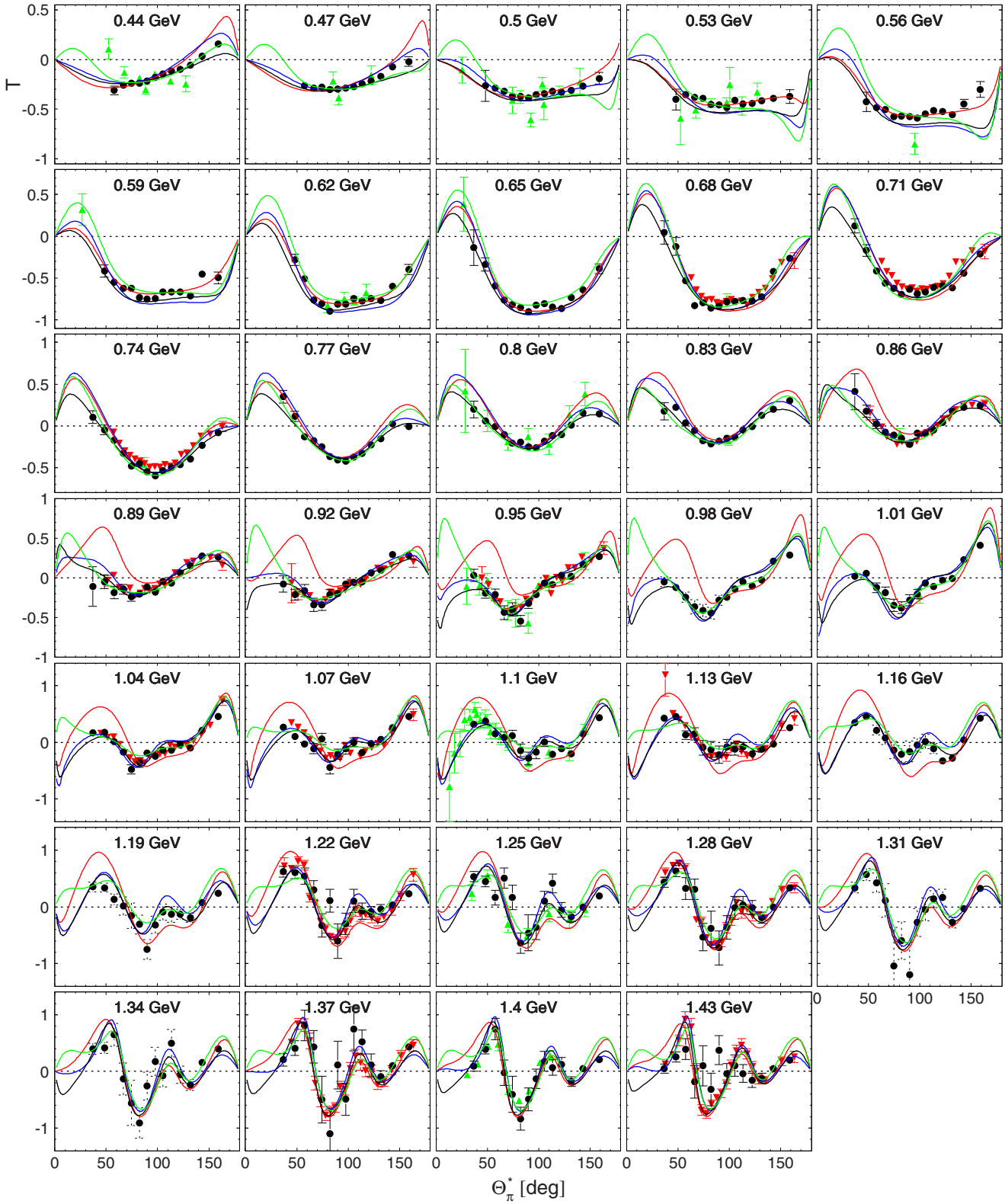

FIG. 6. Target asymmetry T. Our experimental data shown by the filled circles are compared to older data (green triangles) from [20] as well to the latest CBELSA/TAPS data [4] (red triangles). Theoretical predictions of MAID 2007 [21], SAID PR15 [2,22], BG2014-2 [23], and JuBo2015-B [25] models are shown by the red, blue, black, and green lines, respectively. The energy label in each panel indicates the central photon energy for each energy bin. Only statistical uncertainties are given for all data points.

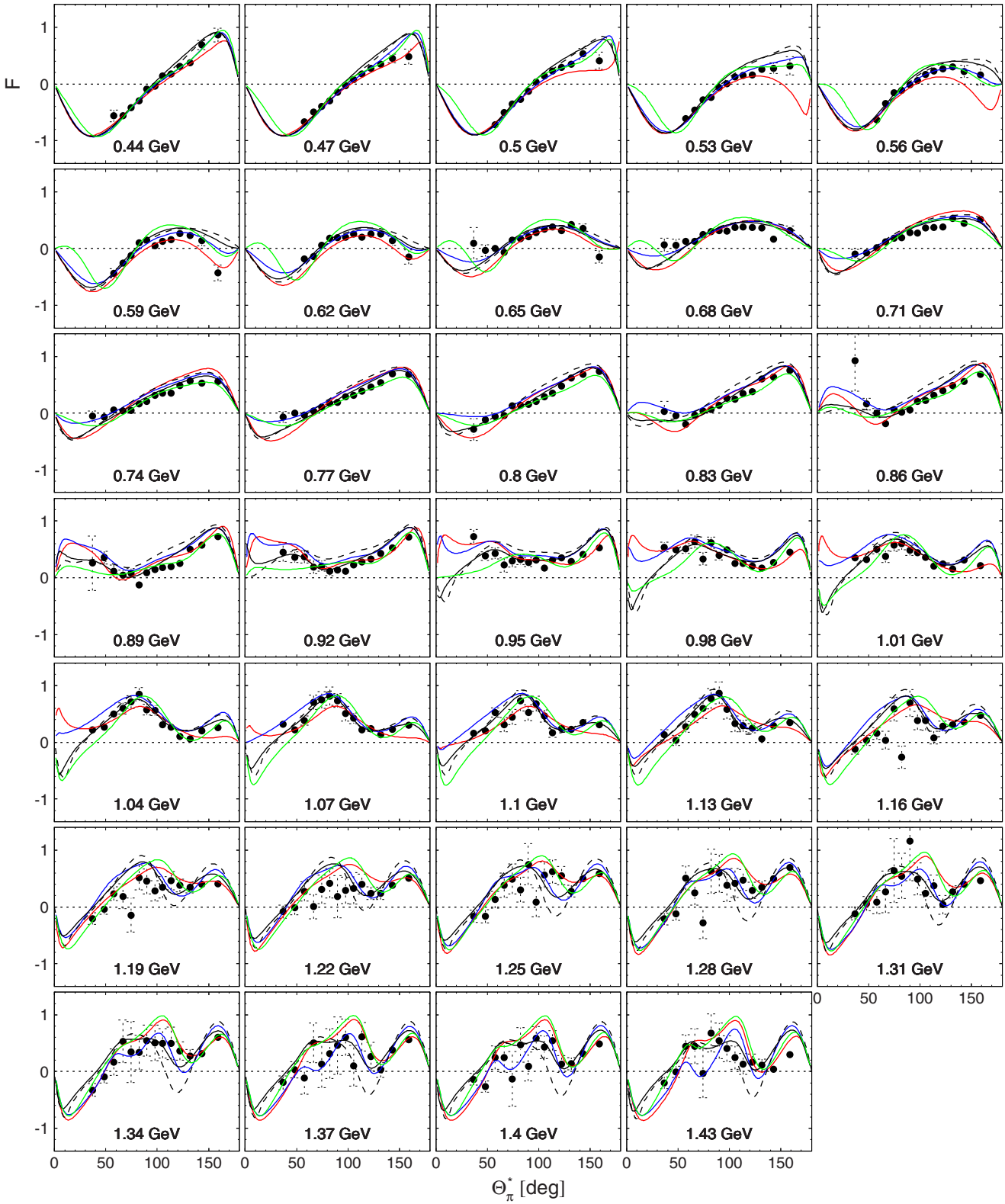

FIG. 7. Beam target asymmetry F. Notations as in Fig. 6. The dashed curve shows the prediction of the BG2011-2 analysis.

The main feature of the coefficients in Figs. 11 and 12 is a rather strong variation of A_1 to A_3 in the region $W =$ 1.50–1.75 GeV and the general smallness of the coefficients A_4 to A_8. A_7 and A_8 are consistent with zero throughout the whole energy range, whereas A_4 to A_6 are rather small but different from zero. This behavior is generally reproduced by all model calculations. Only the JuBo2015-B approach predicts rather large A_4^F and A_5^F coefficients below 1.5 GeV.

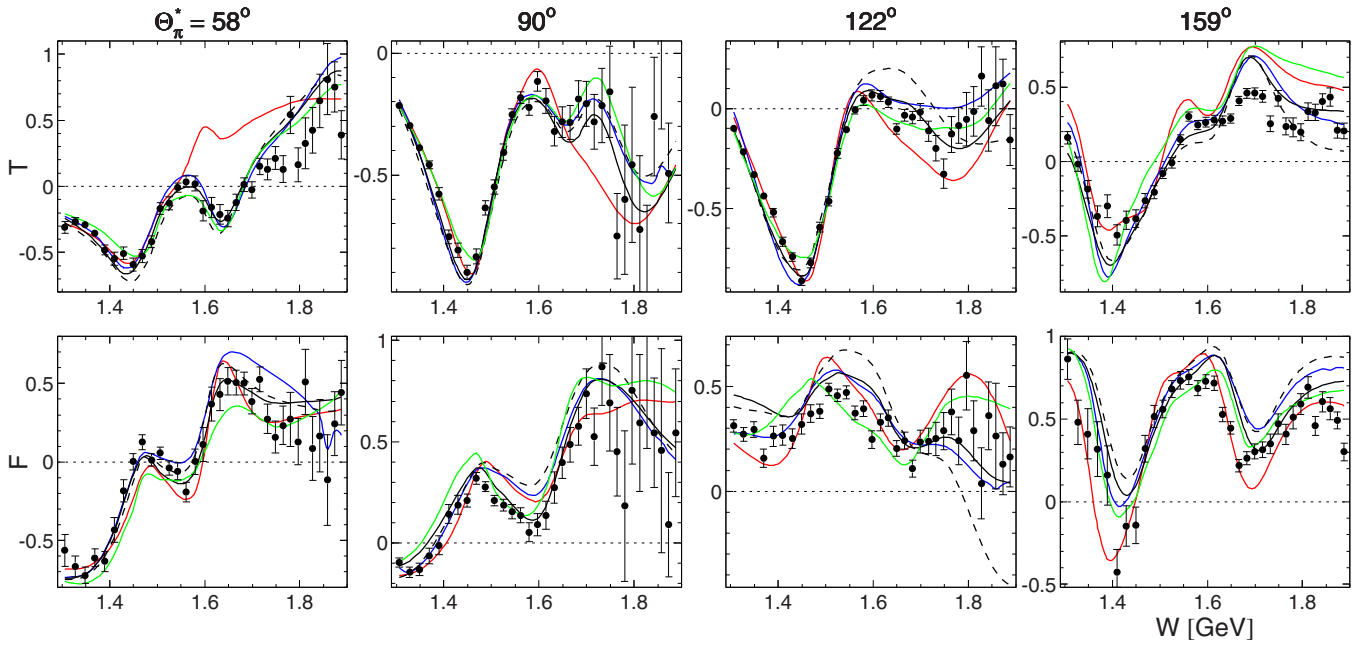

FIG. 8. Dependence of the asymmetries T and F on the center-of-momentum energy W for selected angular bins. The experimental data (filled circles) are compared to theoretical predictions of MAID 2007 (red) [21], SAID PR15 (blue) [2,22], BG2014-2 (black solid) [23], BG2011-2 (black dashed) [24], and JuBo2015-B (green) [25]. Only statistical uncertainties are given for all data points.

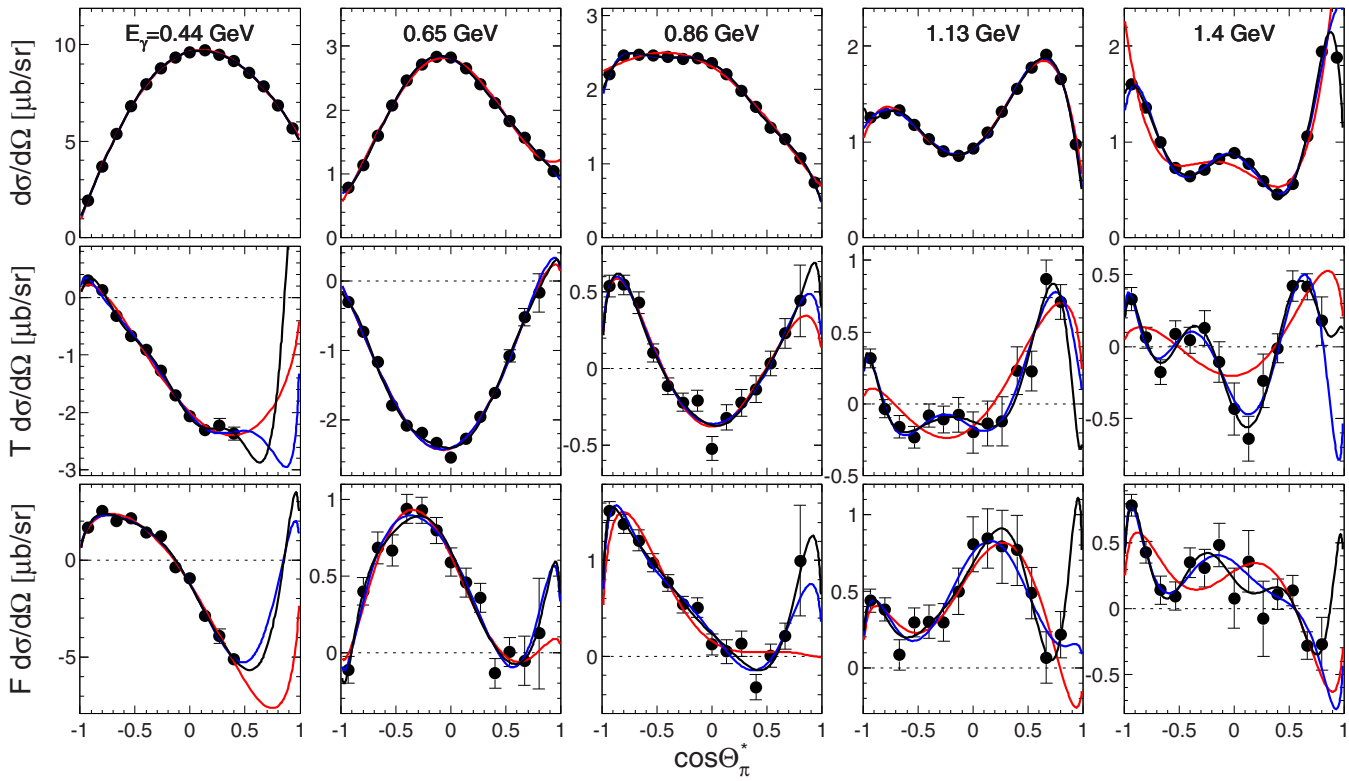

FIG. 9. Unpolarized and polarized differential cross sections of the $\gamma p \to \pi^0 p$ reaction for selected energy bins. Black circles are experimental data. Only statistical uncertainties are indicated. Legendre fit results for the polarized differential cross sections are shown by red ($N = 4$), blue ($N = 6$), and black ($N = 8$) lines.

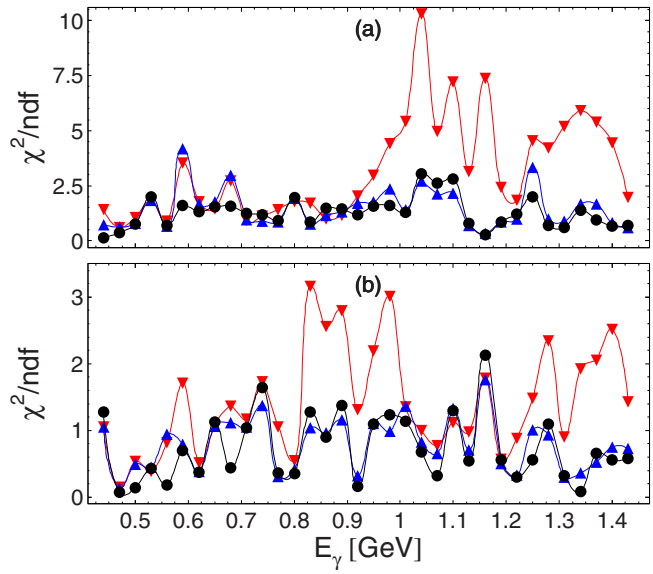

FIG. 10. Energy dependence of the reduced χ^2 values for Legendre fits of the present polarization observables T (a) and F (b) with $N = 4$ (red triangles), 6 (blue triangles up), and 8 (black circles).

The dominant resonance contributions in our energy region come from $N(1520)3/2^-$, $N(1680)5/2^+$, and $\Delta(1700)3/2^-$. The lowest partial waves $1/2^\pm$ are mainly populated by $N(1535)1/2^-$ and $N(1710)1/2^+$, which are not very strongly excited in π^0 photoproduction on protons. The $J^P = 3/2^+$ amplitude, which has a large resonance component saturated by the $\Delta(1232)3/2^+$, is still appreciable in the second and even the third resonance region. Since the pole position of this state is outside our energy region, it can in principle be treated as a background. The same is true for the $7/2^+$ amplitudes populated by the well-established resonance $\Delta(1950)7/2^+$.

According to the selection rules above, the resonance $N(1520)3/2^-$ should influence the coefficient A_2 in the region of 1.5 GeV, whereas $N(1680)5/2^+$ is expected to contribute both to A_2 and A_4 at $W \approx 1.7$ GeV. It is interesting that, although A_2 demonstrates some structure, the coefficient A_4 shows a rather smooth energy dependence around $W = 1.7$ GeV. The structures observed in A_3 at $W = 1.7$ GeV can be explained by the $N(1680)5/2^+$ resonance interfering with another amplitude with spin $J \geqslant 3/2$ and opposite parity. This could be the $\Delta(1700)3/2^-$ or the $N(1675)5/2^-$. The latter is believed to be suppressed in photoproduction on the proton in agreement with quark models [26]. Also in all model calculations the interference of $N(1680)5/2^+$ and $\Delta(1700)3/2^-$ is important; however, a quantitative description of the energy dependence of A_3 around $W = 1.7$ GeV is only possible when additional contributions from background or other resonances are included.

The coefficients $A_6^{T/F}$ should be mainly influenced by the presence of the resonance $\Delta(1950)7/2^+$, which can contribute to $A_6^{T/F}$ by itself and via interference with $N(1680)5/2^+$. The relative smallness of this coefficient shows that this resonance is not strongly excited in the energy region considered. At the same time, a monotonic increase of $|A_6^{T/F}|$ above $W = 1.75$ GeV could be an indication of the increasing role of this resonance at higher energies. Finally, the smallness of the coefficients A_7 and A_8 may be viewed as an indication that no resonances with spin $J = 7/2$ and negative parity, as well as no states with $J > 7/2$, are appreciable in our energy region. However, as discussed above, the reliable determination of the A_7 and A_8 and of high-spin resonance

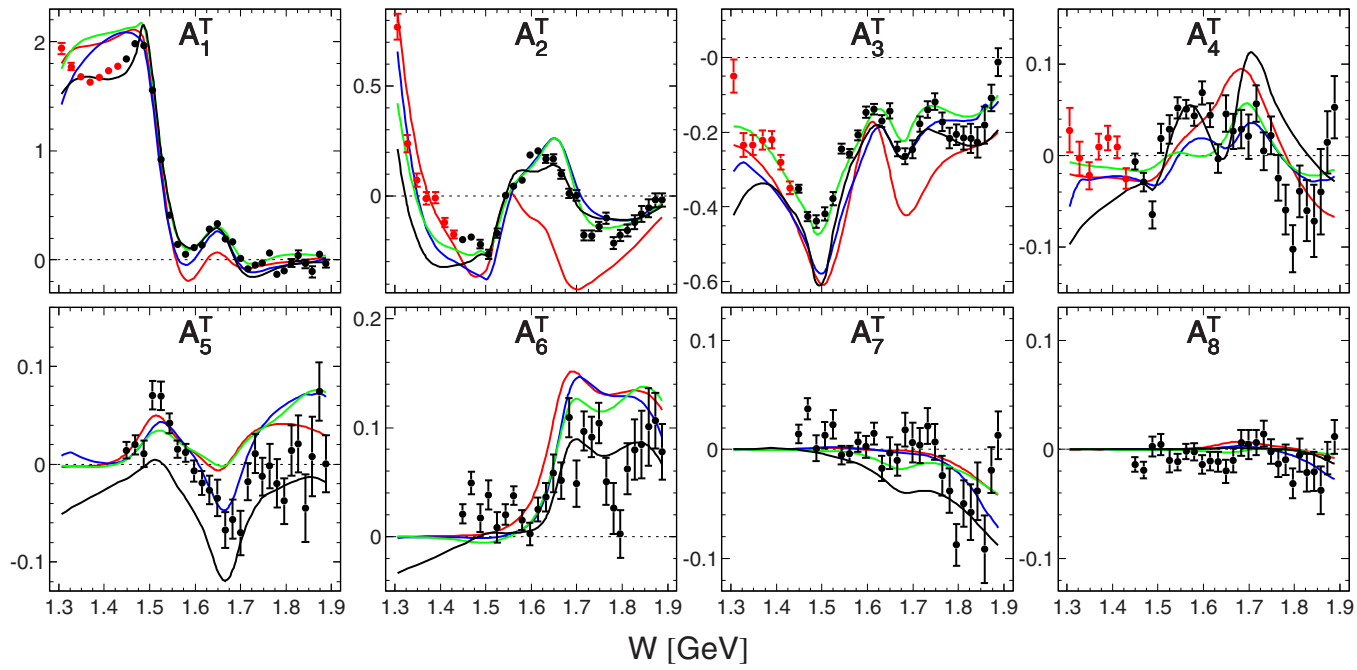

FIG. 11. The coefficients A_n^T in the expansion (5) in units μb/sr obtained from the eighth-order (black circles) and fourth-order (red circles) least-square fits of $T\,d\sigma/d\Omega$ as functions of the total center-of-momentum energy W. Notations for model predictions are the same as in Fig. 6.

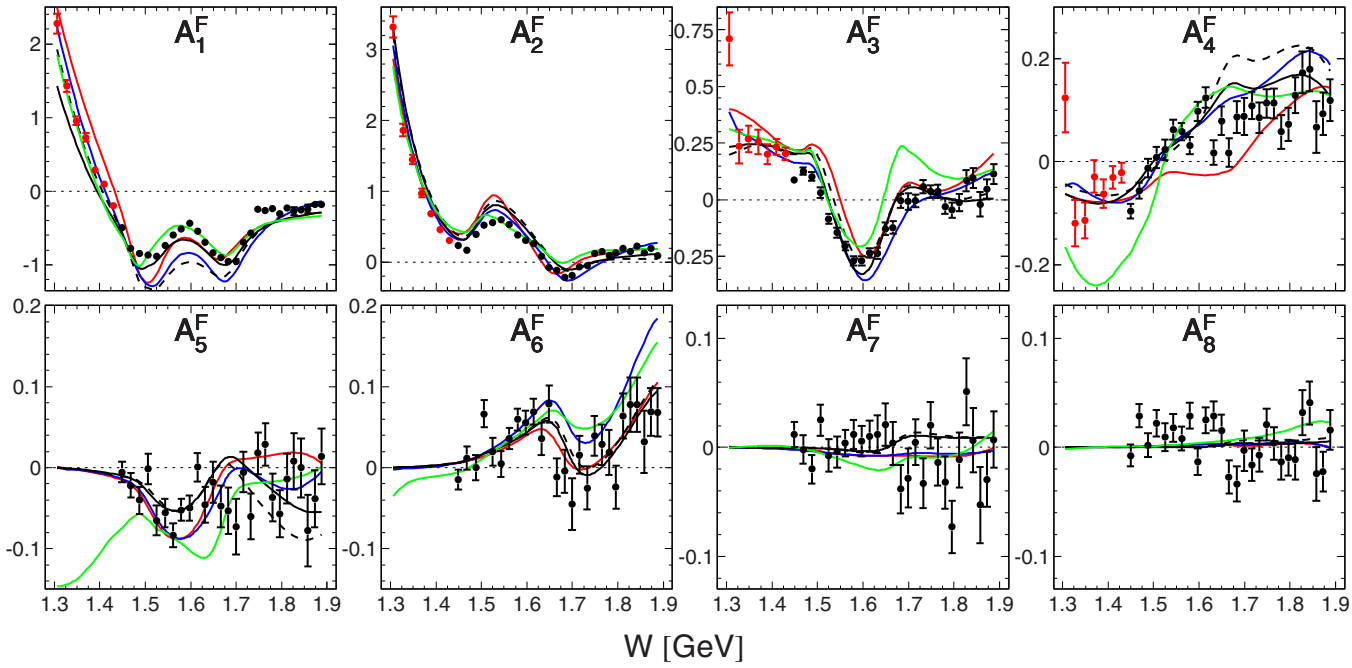

FIG. 12. Same as Fig. 11 for $Fd\sigma/d\Omega$. The dashed curve shows the prediction of the BG2011-2 analysis.

contributions requires new data, in particular in the forward direction.

V. CONCLUSION

We present new experimental results for the transverse target and beam-target asymmetries T and F for the $\gamma p \to \pi^0 p$ reaction. The data were obtained with the Crystal Ball/TAPS calorimeter at MAMI C.

We expand our data in terms of associated Legendre functions. A fit up to order $N = 8$ was used, although $N = 6$ seems to be sufficient to describe the data in almost the whole energy region. Our results show that the rather rapid change of the Legendre coefficients in the second and the third resonance regions can be explained by the presence of the resonances $N(1520)3/2^-$ and $N(1680)5/2^+$ and their interference with $\Delta(1232)3/2^+$, $\Delta(1700)3/2^-$, and $\Delta(1950)7/2^+$ and nonresonant background. Admixtures of states with $J \geqslant 7/2$ seem to be small in our energy region.

The comparison of our data to results of recent model calculations and partial-wave analyses supports the observation that partial-wave amplitudes extracted in different approaches start to converge to model-independent values. This is a success of the huge effort at ELSA, GRAAL, JLab, and MAMI to measure high precision polarization-dependent cross sections and asymmetries. The unique extraction of model-independent partial-wave amplitudes is an important prerequisite for the detailed understanding of the interplay between background and resonance contributions and the precise determination of excited baryon properties.

ACKNOWLEDGMENTS

The authors wish to acknowledge the excellent support of the accelerator group of MAMI. This material is based upon work supported by the Deutsche Forschungsgemeinschaft (SFB 443, SFB 1044); the European Community Research Activity under the FP7 program (Hadron Physics, Contract No. 227431); Schweizerischer Nationalfonds; the UK Sciences and Technology Facilities Council (STFC 57071/1, 50727/1); the US Department of Energy (Offices of Science and Nuclear Physics, Grants No. DE-FG02-99-ER41110, No. DE-FG02-88ER40415, No. DE-FG02-01-ER41194, and No. DE-SC0014133); the National Science Foundation (Grant No. PHY-1039130, IIA-1358175); NSERC FRN: SAPPJ-2015-00023 (Canada); TPU Grant No. LRU-FTI-123-2014; and the MSE Program "Nauka" (Project No. 3.825.2014/K).

[1] V. Crede and W. Roberts, Rep. Prog. Phys. **76**, 076301 (2013).
[2] P. Adlarson *et al.* (A2 Collaboration at MAMI), Phys. Rev. C **92**, 024617 (2015).
[3] A. Thiel *et al.*, Phys. Rev. Lett. **109**, 102001 (2012).
[4] J. Hartmann *et al.*, Phys. Rev. Lett. **113**, 062001 (2014).
[5] J. Hartmann *et al.*, Phys. Lett. B **748**, 212 (2015).
[6] M. Gottschall *et al.*, Phys. Rev. Lett. **112**, 012003 (2014).
[7] O. Bartalini *et al.*, Eur. Phys. J. A **26**, 399 (2005).
[8] S. Strauch *et al.*, Phys. Lett. B **750**, 53 (2015).
[9] M. Dugger *et al.*, Phys. Rev. C **88**, 065203 (2013); **89**, 029901 (2014).
[10] M. H. Sikora *et al.*, Phys. Rev. Lett. **112**, 022501 (2014).
[11] K. Wijesooriya *et al.*, Phys. Rev. C **66**, 034614 (2002).
[12] K.-H. Kaiser *et al.*, Nucl. Instrum. Methods A **593**, 159 (2008).

[13] J. C. McGeorge *et al.*, Eur. Phys. J. A **37**, 129 (2008); I. Anthony *et al.*, Nucl. Instrum. Methods A **301**, 230 (1991); S. J. Hall *et al.*, *ibid.* **368**, 698 (1996).
[14] H. Olsen and L. C. Maximon, Phys. Rev. **114**, 887 (1959).
[15] A. Starostin *et al.* (The Crystal Ball Collaboration), Phys. Rev. C **64**, 055205 (2001).
[16] D. Watts, in *Proceedings of the 11th International Conference on Calorimetry in Particle Physics, Perugia, Italy, 2004* (World Scientific, Singapore, 2005), p. 560.
[17] R. Novotny, IEEE Trans. Nucl. Sci. **38**, 379 (1991); A. R. Gabler *et al.*, Nucl. Instrum. Methods A **346**, 168 (1994).
[18] S. Prakhov *et al.*, Phys. Rev. C **79**, 035204 (2009); E. F. McNicoll *et al.*, *ibid.* **82**, 035208 (2010).
[19] A. Thomas, Eur. Phys. J. Spec. Top. **198**, 171 (2011).
[20] V. G. Gorbenko *et al.*, JETP Lett. **19**, 340 (1974); Sov. J. Nucl. Phys. **26**, 167 (1977); P. Feller *et al.*, Nucl. Phys. B **110**, 397 (1976); M. Fukushima *et al.*, *ibid.* **136**, 189 (1978); P. S. L. Booth *et al.*, *ibid.* **121**, 45 (1977); P. J. Bussey *et al.*, *ibid.* **154**, 492 (1979); H. Herr *et al.*, *ibid.* **125**, 157 (1977); A. Bock *et al.*, Phys. Rev. Lett. **81**, 534 (1998).
[21] The MAID analyses are available through the Mainz website: http://wwwkph.kph.uni-mainz.de/MAID/. See also D. Drechsel, S. S. Kamalov, and L. Tiator, Eur. Phys. J. A **34**, 69 (2007).
[22] The SAID analyses are available through the George Washington University website: http://gwdac.phys.gwu.edu/. See also R. L. Workman, M. W. Paris, W. J. Briscoe, and I. I. Strakovsky, Phys. Rev. C **86**, 015202 (2012).
[23] The Bonn-Gatchina analyses are available through the Bonn website: http://pwa.hiskp.uni-bonn.de/. See also E. Gutz *et al.*, Eur. Phys. J. A **50**, 74 (2014).
[24] A. V. Anisovich *et al.*, Eur. Phys. J. A **48**, 15 (2012).
[25] D. Roenchen *et al.*, Eur. Phys. J. A **51**, 70 (2015).
[26] R. G. Moorhouse, Phys. Rev. Lett. **16**, 772 (1966).